Relationship between tin environment of SnO2 nanoparticles and their electrochemical behaviour in a lithium ion battery

Charlotte Gervillié, Aurélie Boisard, Julien Labbé, Katia Guérin, Sandrine Berthon-Fabry

▶ **To cite this version:**

HAL Id: hal-03080324

https://minesparis-psl.hal.science/hal-03080324

Submitted on 14 Sep 2022

Relationship between tin environment of SnO₂ nanoparticles and their electrochemical behavior in a lithium ion battery

Charlotte Gervillié[1, 2, 3], Aurélie Boisard[3], Julien Labbé[3], Katia Guérin[2*], Sandrine Berthon-Fabry[1*]

1.   MINES ParisTech, PSL University, Centre for processes, renewable energies and energy systems (PERSEE), CS 10207 rue Claude Daunesse, 06904 Sophia Antipolis Cedex, France

2.   Université Clermont Auvergne, SIGMA Clermont, CNRS, ICCF, 24, Avenue Blaise Pascal, 63178 Aubière, France

3.   Safran Tech, SAFRAN, Rue des jeunes Bois, 78117 Châteaufort, France

*Corresponding authors:

Sandrine Berthon-Fabry: E-mail Address [sandrine.berthon-fabry@mines-paristech.fr]

Katia Guérin: E-mail Address [katia.araujo_da_silva@uca.fr]

Abstract

SnO_2 nanoparticles were synthetized in three different ways (solvothermal, hydrothermal, sol-gel) and heat-treated under argon at 600°C to obtain different physico-chemical characteristics (texture, structure and surface chemistry) determined by X-ray powder diffraction (XRD), infrared spectroscopy (FTIR), ^{119}Sn solid state Nuclear Magnetic Resonance (NMR), Electron Spin Resonance (ESR), scanning electron microscopy (SEM) and 77K nitrogen sorption. When used as electrode material in a lithium ion battery, their electrochemical properties were evaluated by galvanostatic measurements. Among crystallinity, particle size, specific surface area and associated porosity, hydroxyl groups and paramagnetic centers, only the last two parameters appear as determinants of electrochemical performance. Solvothermal and hydrothermal syntheses lead to the presence of certain hydroxyl groups in the oxide whereas sol-gel one prevents their formation but forms paramagnetic species. The hydroxyl groups favour a good coulombic efficiency and an interesting reversibility of the conversion process. Paramagnetic species limit the electrochemical process. Their elimination by a heat-treatment at 1000°C under argon improves the electrochemical properties. Understanding the key factors to favour SnO_2-based materials allows to obtain capacities of about 900 $mAh.g^{-1}$ over 5 cycles.

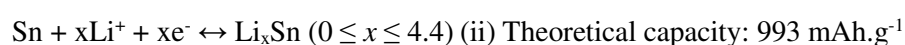*Keywords*: SnO_2, lithium-ion battery, hydroxyl groups, paramagnetic centers, electrochemical performance

1. Introduction

Currently lithium-ion batteries are used mainly for mobile electronic devices (such as cellular phone, laptop etc.…). This technology seems to be the most advanced battery technology due to its

high capacity and environmental friendliness compared to other types of batteries [1]. However, they are limited in terms of energy density. For this improvement, industrial and academic research has focused on how to obtain new materials with a higher capacity or a higher/lower operating voltage compared to Li^+/Li for positive/negative electrode materials, respectively. [2]. Today, battery capacities are limited by the low gravimetric capacity of the positive electrode. Rapid improvements in this electrode require equally important research on negative materials. For a long time, the ideal materials for negative materials were those capable of intercalating lithium ions into their structure. They had to meet several criteria such as high electron conductivity, large particle size, chemical stability, rapid diffusion of lithium ion, low cost and absence of toxicity. Graphite met all these requirements and became the most commercially available material for use as a negative electrode. Nevertheless, with a theoretical capacity of 372 $mAh.g^{-1}$ and its safety issues, it appears to be limiting for new-targeted applications. Over the last ten years, new approaches have been trying to get rid of these criteria. "Alloy" and "conversion" materials can contain more lithium and therefore have very high capacities (theoretically up to 3578 $mAh.g^{-1}$ for silicon, 993 $mAh.g^{-1}$ for tin and 663 $mAh.g^{-1}$ for antimony) [3–5].

Tin dioxide (SnO_2) has been studied in a large range of fields due to its semiconductor behaviour combined with its good mechanical and thermal stability. This diversity of applications is related to the number of morphologies (3D, 2D, 1D), particle sizes (nanometric, micrometric), phases (Rutile, $CaCl_2$ type), surfaces and crystallinity (possible defects) of tin dioxide. It is of great interest for energy storage because it combines both the electrochemical properties of tin and better stability as a negative electrode compared to alloy materials. In the first conversion step, tin is formed and lithium is bonded to oxygen (i). This step is described in the literature as irreversible. The tin is

then engaged in a redox process while the Li_2O no longer reacts but acts as a buffer moderating the large volume change during the formation of tin-lithium alloys [6]. The second step is the formation of the tin-lithium alloys (ii). Tin forms up to seven alloys with an increased amount of lithium: Li_2Sn_5, $LiSn$, Li_7Sn_3, Li_5Sn_2, $Li_{13}Sn_5$, Li_7Sn_2 and $Li_{22}Sn_5$ [7]. The electrochemical reactions mentioned in the literature are as follows [8,4]:

$$SnO_2 + 4Li^+ + 4e^- \rightarrow Sn + 2Li_2O \qquad \text{(i) Theoretical capacity: 711 mAh.g}^{-1}$$

$$Sn + xLi^+ + xe^- \leftrightarrow Li_xSn \ (0 \leq x \leq 4.4) \text{ (ii) Theoretical capacity: 993 mAh.g}^{-1}$$

Unfortunately, the industrial use of SnO_2 as electrode material is limited by three effects [6,9,10]: the enormous irreversible capacity in the first cycle caused by the formation of a solid electrolyte interface (SEI) and by the formation of Li_2O (i), the alloying and de-alloying of lithium with tin further creating a major volume change in the tin crystal structure, the progressive loss of capacity due to the aggregation of tin particles into inactive clusters during the cycle.

Various means have been used to overcome these problems. The nanostructurating of SnO_2 has been widely studied [11], as nanosizing reduces internal stresses during volume change and improves the capacity and lifetime. Indeed, particle size reduction reduces the diffusion /transport lengths of ions and electrons and increases conductivity and capacity. In addition, it has been reported that the first reaction (i) is partially reversible in the case of very small SnO_2 nanoparticles [12–14]. In addition, nanosizing can limit or even suppress the coarsening of Sn [14]. Another strategy is the synthesis of carbon/tin composites. The purpose of adding carbon is to increase the electronic conductivity of the electrode and prevent the coalescence of tin particles. Numerous studies have demonstrated the role of carbon in structures such as SnO_2/carbon nanotubes [15], SnO_2/carbon aerogel [16] and SnO_2/graphene [17]. However, the incorporation of nanocarbons

reduces volumetric and gravimetric energy densities as with any composite with an inactive electrochemical matrix. Thus, before working on nanocomposites, the intrinsic behaviour of tin oxide particles must be fully understood in order to further optimize the composite. Indeed, many different tin oxide nanomaterials have been synthesized and evaluated to minimize volume changes and increase lithium transport: for example, spherical particles (OD), nanorods or nanotubes (1D), nanoplates (2D), and nanoflowers or aerogels (3D) [11]. Sun et al. have shown that the synthesis of porous or hollow SnO_2 structures can also absorb some of the volume expansion due to the hollow spaces that make them up [18]. These different SnO_2 nanomaterials have been prepared by various methods such as hydrosolvothermal synthesis, template synthesis and sol-gel synthesis [19]. Hu et al. demonstrated that the electrochemical process could be highly reversible for well nano-structured SnO_2 anode. They used a thin-film electrode, which allowed them to achieve a high initial coulombic efficiency of 95.5% [14]. Using high-resolution microscopy (HREM), Retoux et al. demonstrated the decomposition of SnO_2 crystallites into tin grains 10 to 50 nm wide during the first cycle. However, during the cycle, the tin grains grew from 40 nm to an average value of 110 nm after 500 cycles [20]. For nanostructured SnO_2, Kim et al obtained a long life cycling of up to 600 mA.g^{-1} after 100 cycles. They emphasized the importance of bonding strength by using fine structure X-ray absorption spectra and calculation of the bonding strength [13]. Focusing on nanostructurated SnO_2, the best electrochemical properties have so far been achieved by a sacrificial template method using hydrothermal plus heat- treatment at 500°C. The SnO_2 had a capacity of 695 mAh.g^{-1} when the current density was 100 mA g^{-1}. After being tested at a higher current density of 1.0 A g^{-1} over 100 cycles, a capacity of 602 mAh.g^{-1} was maintained. The superior performance of porous SnO_2 can be attributed to the porous and hollow microstructure of

the 16 nm diameter particle size [21].

The literature on SnO_2 is considerable and leads to a lot of data based on each type of SnO_2. Some physico-chemical parameters seem to be key factors in increasing performance such as crystal structure, particle size, shape, hydroxyl content and Sn-O binding strength. The problem is that none of these papers have compared different nanostructurating methods and correlated electrochemical properties obtained under the same experimental conditions. Thus, in this work, first to form nanostructured particles of 10-50 nanometers, but also to modulate surface chemistry, crystallinity and porosity, three nanostructuration ways were chosen (sol-gel, hydrothermal and solvothermal ones) and the materials obtained were fully characterized in order to correlate their physico-chemical properties with their electrochemical ones implemented in the same way.

2. Experimental

2.1 Synthesis of SnO_2

Three synthesis pathways, capable of obtaining materials with a size of about 20 nm, have been chosen. This size was reported to be the size stabilized size after electrochemical milling. In order to reduce the energy consumed by this grinding during the first cycles, we chose to work with SnO_2 nanomaterials. Then, a heat-treatment at 600°C under nitrogen for 3 hours allowed us to carry out the first synthesis in order to promote an increased crystallinity without huge increase in particle size. Indeed, Diéguez et al. showed that the size of SnO_2 nanoparticles in sol-gel powders evolves from 3 to 100 nm according to the two growth rates of the heat-treatment with a weak evolution below 400°C (8.10^{-3} nm.°C^{-1}) and a faster evolution after (14.10^{-2} nm.°C^{-1}). In addition,

this heat-treatment condition was imposed because the electronic conductivity of semiconductors is related to the periodic crystal structure. At only 60°C, the crystallinity is low and the material remains partially amorphous [22,23].

2.1.1 Sol-gel method

Aerogel has been synthesized following the work of Ozouf et al. [24]. Tin isopropoxyde and nitric acid (35%), were purchased from Alfa Aesar. Two solutions were prepared (A and B). Solution A is prepared by mixing tin isopropoxyde (4.967 ml) with isopropanol (5 ml). Solution B is prepared by mixing nitric acid (HNO_3, 0.05 mL), deionized water (0.076 mL) and isopropanol (iPrOH, 3.967 mL) while mixing under magnetic stirring. Solution B is added dropwise to solution A with stirring magnetically. To avoid the surface drying, the resulting gel is covered with isopropanol for ageing during 48 hours at room temperature. After ageing, the gel is washed by immerging it in isopropanol three times a day for two days to remove impurities and residual water. The gel is then autoclaved and dried with a CO_2 supercritical drying at 80 bar, 37 ° C during 4 hours (15 kg of CO_2) to obtain the aerogel. The material is then heat-treated in air at 600 °C for 5 hours with a 5 °C.min^{-1} ramp.

2.2.2. Hydro-solvothermal methods

The SnO_2 nanoparticles were prepared by hydro-solvothermal method. Under magnetic stirring, 4.6 g of tin tetrachloride pentahydrate ($SnCl_4.5H_2O$) from Acros Organics was dissolved in 35 mL distilled water. Then 35 mL NaOH solution (2M) was added, and finally 70 mL ethanol were added to obtain a water/ethanol solvent mixture of (25/75 % by weight). The pH of the solution was

adjusted using the NaOH solution (2M) until the pH was 11-12. The mixture was then transferred to a 150 mL Teflon-linked stainless steel autoclave and kept at 180°C for 24 hours. After cooling to room temperature, the precipitates were collected and washed with a deionized water/ethanol mixture (50/50 % by weight) by centrifugation until pH=7. The solid obtained was air-dried at 60°C for 12 hours and then heat-treated at 600°C for 5h with a 5 °C.min^{-1} ramp.

For the hydrothermal synthesis, the same experimental procedure is followed as for solvothermal but ethanol is replaced by distilled water in the solvent mixture.

2.2 Physico-chemical characterizations

The structure of the prepared samples was determined by X-ray diffraction (XRD) using a X'pert pro diffractometer with a Cu Kα radiation source between 20 and 90°. The X-ray diffractograms were analyzed by the Rietveld method in the FullProf program. FTIR spectra were collected with a Bruker 27 tensor spectroscope. The NMR experiments were carried out with a Bruker Advance spectrometer, with working frequencies for ^{119}Sn of 111.85 MHz. A Bruker Magic Angle Spinning Probe (MAS) operating with 2.5 mm rotors was used. For the MAS spectra, a simple sequence was performed with a single $\prod/2$ pulse length of 3.5 μs. The chemical shifts of ^{119}Sn were externally referenced to commercial SnO_2 (Tin (IV) oxide nanopowder from Sigma Aldrich) whose chemical shift is known as being at -604.3 ppm [25]. The chemical shift of the commercial SnO_2 has been fixed at this value. The Electron Spin Resonance (ESR) spectra of the powder samples were recorded on a Bruker ADVANCE spectrometer at 298 K. Measurements were made using a resonance frequency of 9.8 GHz, a magnetic field modulation of 100 kHz, a modulation amplitude

(Hm) of 4 G, and a microwave power of 2.172 mW (298 K). The variation in amplitude Hm was used to separate the EPR signals from the noise. (2,2)-Diphenyl-1-Picrylhydrazyl (DDPH) was used to calibrate the g-factor.

The texture of the materials has been characterized by 77K nitrogen isotherms to determine the Brunauer-Emmett-Teller (BET) parameter and pore size distribution by DFT methods on the desorption branch, using an ASAP 2020 surface area analyzer from Micromeritics Instrument Corporation. Total pore volume is measured at $p/p^0 = 0.995$. The analysis was performed on samples with were pre-treated at 200°C under secondary vacuum (up to 10^{-6} mbar) for 6 hours to remove adsorbed species. The quantity of material used for the measurement was set to obtain a surface area greater than 10 m^2. The porosity was calculated using DFT theory. The total pore volume was determined at p/p equal to 0.99. The ZEISS SUPRA 40 scanning electron microscopy (SEM) operating at 3 kV was also continued. For transmission electron microscopy (TEM) observations, the samples were first crushed, then dispersed in methanol and deposited on a carbon grid. The observations were performed using a JEOL 2100F microscope operated at 200kV in multibeam conditions at low magnification and high resolution for high magnification.

2.3 Electrochemical characterizations

The electrochemical properties of tin oxide material were evaluated at room temperature in CR2032 coin cells with lithium metal as the negative and reference electrode. The working electrode was composed of 70 w/w% of prepared active material, 20% conductive agent (Y50 from Imerys Graphite & carbon) and 10% binder (PVDF (Polyvinylidene Fluoride) HSV900 from ARKEMA). A sandwich of CELGARD 2400/Whatman glass fiber/CELGARD 2400 as a separator

was saturated with 1M LiPF$_6$ EC:PC:DMC (Ethylene carbonate: Propylene carbonate : Dimethyl carbonate) (1:1:3 v/v) mixture electrolyte. The mass loading of the anode active materials was as nearer as 2 mg.cm^{-2}, in agreement with classical data insuring good performances of conversion materials [26]. The coin cells were assembled in an argon-filled glove box. For the galvanostatic measurements, the cells were discharged and charged at a constant current of 10 mA.g^{-1} between 3 and 0.05 V vs. Li$^+$/Li with a Biologic potentiostat. The results presented were obtained almost three times.

## 3. Results and Discussion

3.1 Structural characterizations

The XRD patterns of the resulting materials, as shown in Figure 1, can be fully indexed to the rutile structure with a P4$_2$/mnm space group characteristic of SnO$_2$ (JCPDS no. 41-1445, a$_{th}$ = 4.738 Å, c$_{th}$ = 3.187 Å). No impurities were detected. The SnO$_2$ aerogel (c) has the sharpest peaks, meaning that the sample has a better degree of crystallization than samples based on the solvothermal (a) and hydrothermal (b) methods. Using the Rietveld method, the cell parameters of the obtained materials were refined and the size of the Scherrer crystallites was calculated for peaks 110 and 101 according to the formula:

$$d = \frac{k.\lambda}{H.cos\theta}$$

with d: Crystallite size, k: Correction factor (k=0.89), λ: Incident wavelength (1.5408 Å), H: Full width at half maximum (°), θ: Incident angle (°).

All crystalline parameters have been given in Table 1. The cell parameters calculated using Le Bail refinements confirm the crystal structure and size of rutile SnO$_2$. The crystallites appear to grow

more slowly for hydro-solvothermal treatment (about 4.8 nm) than for sol-gel treatment (10.5 nm).
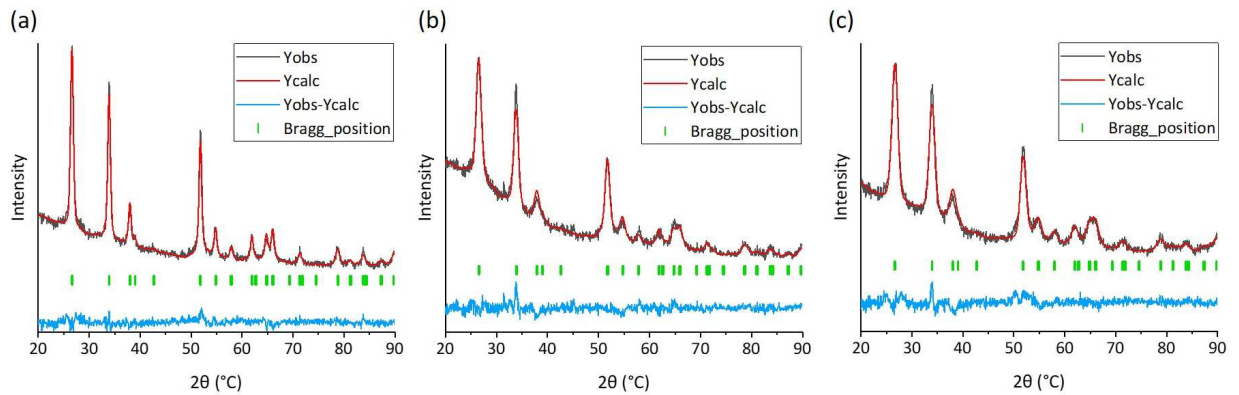
Figure 1 : XRD powder pattern profiles and Le Bail refinements of SnO_2 nanoparticles obtained

by (a) sol-gel, (b) hydrothermal and (c) solvothermal syntheses.

Table 1 : Cells parameters calculated owing to the Rietveld method, correlated Scherrer crystallite

sizes.

	a = b (Å)	c (Å)	Chi2	Crystallite size (nm)	
				d_{110}	d_{101}
SnO_2	4.7400	3.1900	/	/	/
Solvothermal SnO_2	4.7458	3.1885	2.00	14.2	18.7
Hydrothermal SnO_2	4.7381	3.1841	2.39	12.0	15.3
Sol-gel SnO_2	4.7379	3.1871	2.06	27.8	30.7

3.2 Textural characterizations

The morphology of the as-prepared SnO_2 was observed using a SEM, as shown in Figure 2. It

was found that the different syntheses lead to different morphologies of the samples. For SnO_2

synthesized by the solvothermal method, the particles are elongated into nanorods and aggregated

into nanoflowers-like clusters (Figure **2**a). For SnO_2 synthesized by hydrothermal treatment, the particles are spherical and agglomerated into porous spherical clusters larger than 100 nm (Figure **2**b). Sol-gel synthesis allows interconnection of spherical particles (Figure **2**c).

Figure **2** shows also the transmission electron microscopy (TEM) of the as-prepared SnO_2. For the solvothermal SnO_2, nanorods are observed with a major axis oriented along <001>. They have an average length of 17.6 ± 1.2 nm and a width of 7.0 ± 0.4 nm. The nanorods appear to be independent of each other. Vasquez et al. also shown experimentally that the use of ethanol promotes the self-assembly of particles into "flower" type morphologies composed of nanorods shaped nanoparticles [27].

For hydrothermal SnO_2, the particles are spherical with an average diameter of 10.8 ± 1.0 nm. The material revealed a wide grain size distribution. The grains are connected to each other. For sol-gel synthesized material, the TEM images showed crystals with homogeneous size connected to each other. The average size of the grains is 16.6 ± 0.5 nm.

The (110) plane of SnO_2 (densest plane of the rutile structure) is equal to d = 0.335 nm. The same distance is found for the other samples, the difference is in the measurement error.

The average particle size observed with TEM and the aggregate size observed with MEB are summarized in Table 2.

For all three materials, TEM images indicates that the particles are composed of one crystallite. Courtney et al. have shown that minimizing the size of the crystallites of the starting SnO_2 leads to minimizing the particle size of the tin formed after conversion. The control of the crystallite size would then make it possible to avoid the coexistence of two phases during the insertion of lithium and thus to avoid too important structural changes [28]. In agreement with this result, Campet et al.

pointed out that by minimizing the crystallite size, the formation of defects would be favored. These defects will then serve as grafting sites for lithium. The cation-anion bond will be weakened allowing the insertion of lithium with a more favorable structural rearrangement [29]. According to these postulates, the hydrothermal-C600 material has the smallest crystallite size and therefore the most favorable for electrochemical performance.
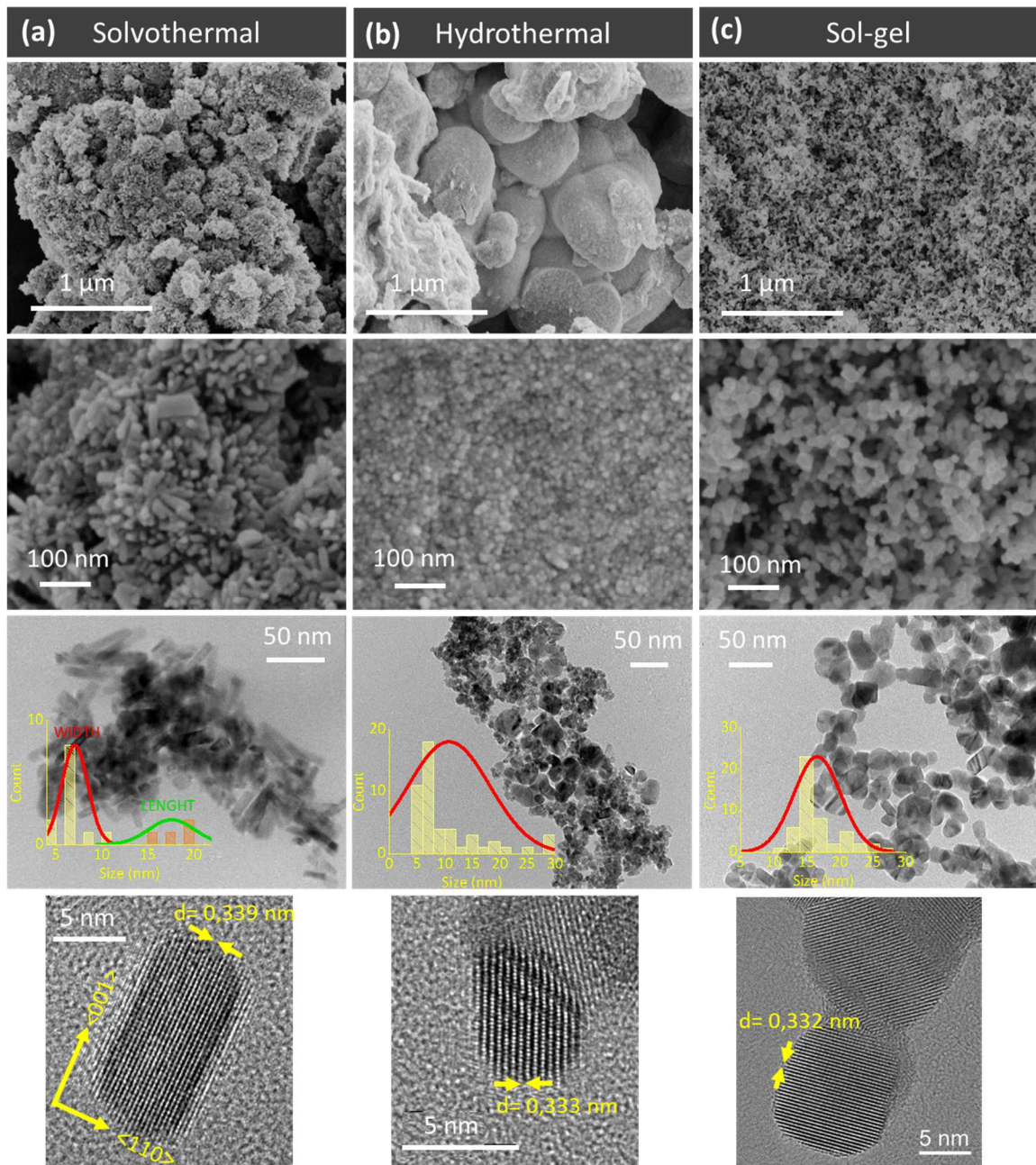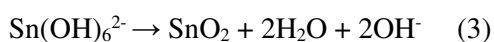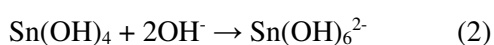

Figure 2 : SEM and TEM images and particles size distribution of SnO_2 nanoparticles prepared by

(a) solvothermal, (b) hydrothermal and (c) sol-gel syntheses

Table 2 : Observed particles size by TEM and textural properties obtained by N_2 sorption of SnO_2 particles prepared under various conditions.

	Particle size (nm)	Aggregate size (nm)	BET SSA $(m^2.g^{-1})$	Volume of micropores < 2 nm $(cm^3.g^{-1})$	Volume of mesopores [2- 50 nm] $(cm^3.g^{-1})$	Total porous volume $(cm^3.g^{-1})$
Solvothermal SnO_2	L: 17.6 ± 1.2 W: 7.0 ± 0.4	~ 100	44.2 ± 0.3	0.005	0.072	0.077
Hydrothermal SnO_2	10.8 ± 1.0	~ 750	47.6 ± 0.2	0.005	0.057	0.060
Sol-gel SnO_2	16.6 ± 0.5	~ 30	35.1 ± 0.1	0.003	0.029	0.089

The mechanism of formation of these three different morphologies is clearly different. In the solvo-hydrothermal method, SnO_2 nanoparticles are formed by precipitation. First, the dissolution of the salt precursor $SnCl_4.5H_2O$. When NaOH is added, a white slurry is observed, indicating the beginning of the formation of $Sn(OH)_4$ (equation 1), followed by the formation of $Sn(OH)_6^{2-}$ (equation 2). During heat-treatment, nuclei form spontaneously through the condensation reaction (equation 3). As a result of the Ostwald maturation phenomenon, the nuclei have aggregated. Eventually, the nanoparticles are assembled in their final form [11,18,30].

$$Sn^{4+} + 4OH^- \rightarrow Sn(OH)_4 \qquad (1)$$

$$Sn(OH)_4 + 2OH^- \rightarrow Sn(OH)_6^{2-} \qquad (2)$$

$$Sn(OH)_6^{2-} \rightarrow SnO_2 + 2H_2O + 2OH^- \qquad (3)$$

This last step depends on the overview parameters. Ethanol controls particle nucleation and growth

in a different way [31]. The polarity of the solvent is higher, so fewer hydrogen atoms can participate by hydrogen bonding. The electron of the anion is more readily available for the reaction due to the lack of stabilization by the solvent. The nucleation density is higher. As a result, the probability that the primary particles will encounter neighbouring particles is also higher. It has been reported that the surface free energy of crystalline SnO_2 follows the order (001) > (101) > (100) > (110) leading to the formation of nanorods [30]. In sol-gel synthesis, the mechanism is totally different. First, a sol is created when water is added to the metal alkoxide. It consists of a dispersion of nanoscale colloidal oligomers. Then, the sol will go through different reactions such as hydrolysis, condensation and polymerization to form a gel. This gel is a three-dimensional network of particles in which the solvent is trapped.

The particle size for the hydro-solvothermal treatments is much larger than the size of the corresponding crystallites, indicating that the particles were clustered. Instead of the other synthesis, the crystallite size of the aerogel is larger than that of the other synthesis. This observation confirmed the better organization of the aerogel compared to the other materials.

Textural characterization of the SnO_2 samples was performed using N_2 at 77K adsorption isotherms. The sample surface areas are reported in Table 2 and the isotherms and pore size distributions (PSD) are shown in Figure 3. For aerogel, the hysteresis loop at high relative pressure without a final plateau and the type IV isotherm shown in Figure 3c are characteristics of predominantly mesoporous materials. The pore volume due to pores larger than 50 nm is mainly due to interparticle porosity according to SEM observations. At low relative pressure, few micropores can be observed. The main volume is due to mesopores that are observed centred at 30 nm. The specific surface area (35 m².g^{-1}) is smaller than for other materials and is related to the larger

particle size. This value corresponds to the theoretical mean particle diameter of 52 nm calculated

for non-porous spherical particles based on the following formula and is in agreement with the

SEM.

Formula (1): $SSA = \frac{6 \times 1000}{\Phi \times d}$ with surface specific area SSA (m².g^{-1}), Φ, diameter (nm), density

(g.cm^{-3}) with d_{SnO2}=6.95 g.cm^{-3} (for the rutile structure).
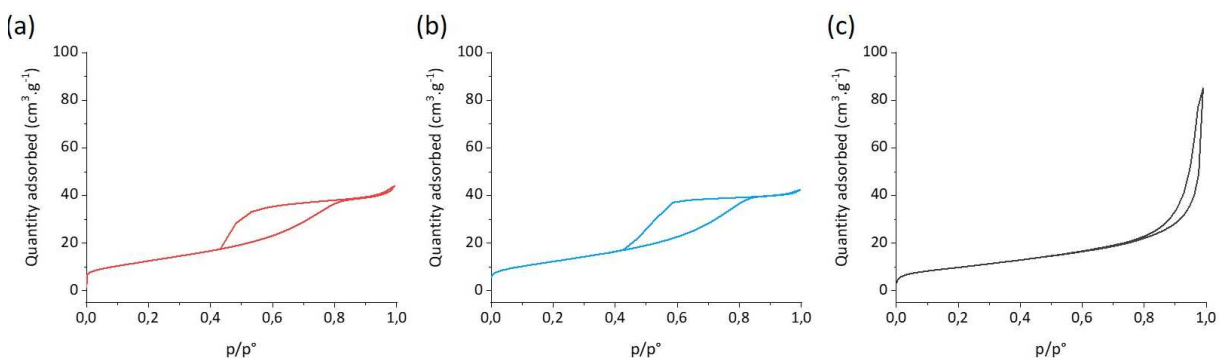

Figure 3: 77K N$_2$ isotherms of (a) solvothermal, (b) hydrothermal and (c) sol-gel syntheses.

The solvothermal material has a type IV isotherm with a H3 loop as shown in Figure 3a. This

hysteresis loop is characteristic of very elongated cavities of different sizes with a rigid porosity.

The specific surface area (48 m².g^{-1}) is correlated with the smallest particle sizes (theoretically 16

nm with formula 1) confirmed by SEM observations. The hysteresis loop of hydrothermal material

shown in Figure 3b is characteristic of type IV isotherm with H2 loop when the sample has

interconnected pores of different sizes and shapes [32]. The remaining porosity is at the macropore

scale (> 140 nm) observable by SEM and not analyzed by this technique. Although the particle

arrangement is different from that of the solvothermal material, the particles size is approximately

the same, leading to the same specific surface area (47 m².g^{-1}).

3.3 Tin environment characterizations

The size of the particles for all the SnO_2 materials is nanometric. Many structural defects are therefore possible for these compounds. In a real environment, a surface will more often become accustomed to chemical impurities and adsorbed atoms. These surface or interface defects are responsible for surface states with a varied energy spectrum. These defects can then influence physico-chemical properties such as electronic conductivity [33] and electrochemical activity [34]. It seems then necessary to pay great attention to them.

The Fourier transform infrared (FTIR) spectra shown in Figure 4 show the peaks of the prepared SnO_2 materials. The very wide adsorption peak between 670 and 480 cm^{-1} can be assigned to the Sn-O and Sn-O-Sn bonds. The peak at 1360 cm^{-1} can be attributed to Sn bound to surface hydroxyls (δ_{OH}(Sn–OH)) [35,36]. This latter band is present only in hydro-solvothermal samples. At 1630 and 3420 cm^{-1}, contributions of water adsorption occur. The sol-gel material does not contain OH groups whereas this is the case for the other two syntheses.
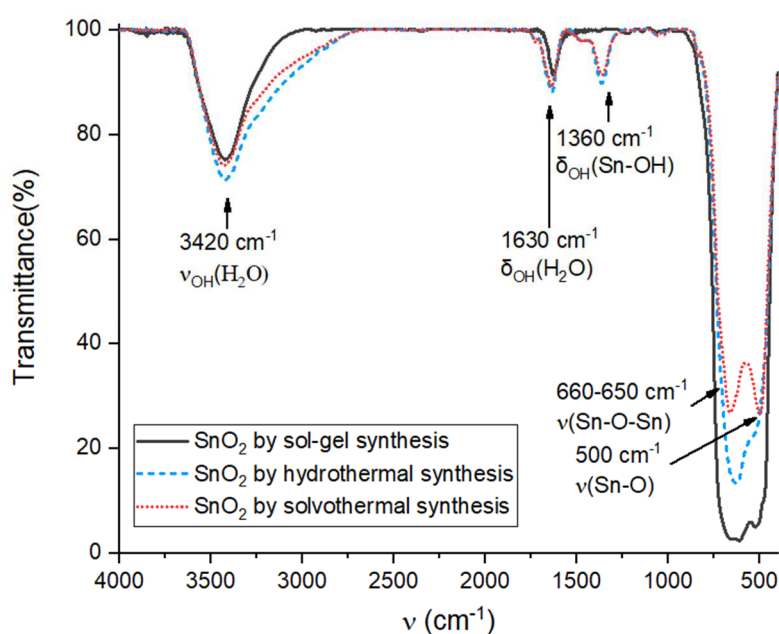
Figure 4 : Infrared spectra of spectra of solvothermal, hydrothermal and sol-gel SnO_2 materials
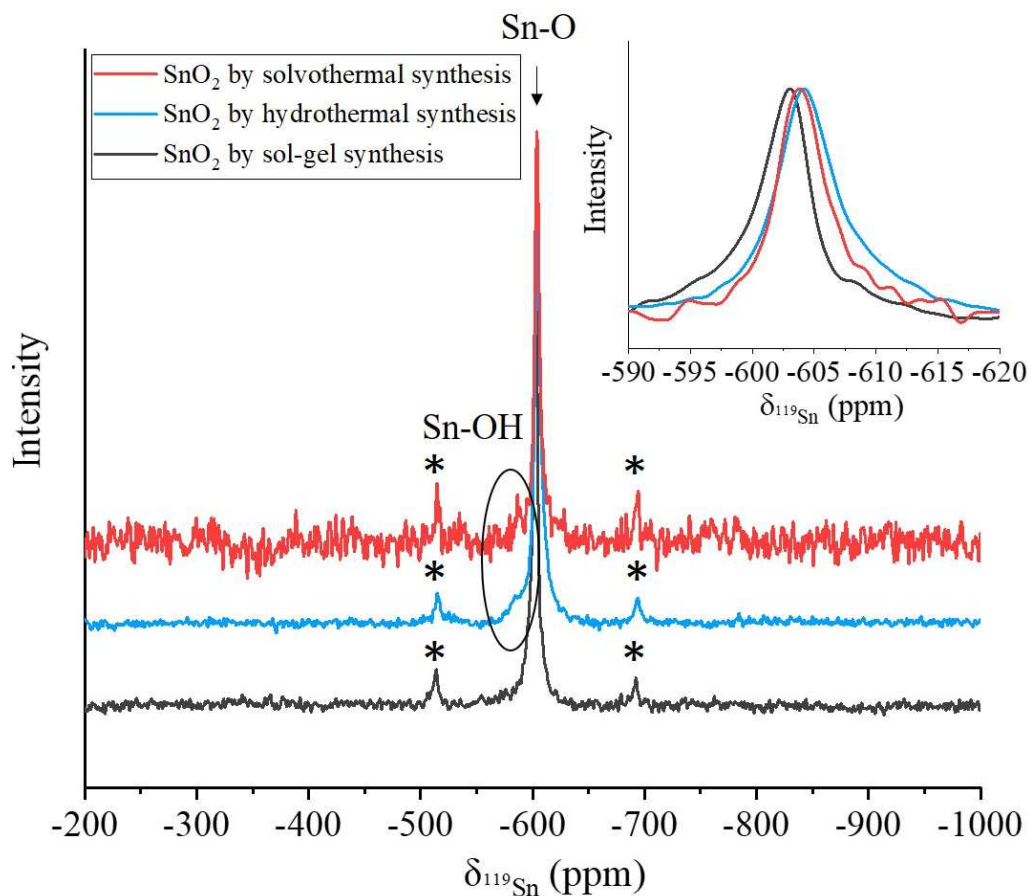
Figure 5 : ^{119}Sn solid-state NMR spectra of solvothermal, hydrothermal and sol-gel SnO_2, with spinning sidebands denoted *.

Table 3 : NMR values for SnO_2 obtained by solvothermal, hydrothermal and sol-gel syntheses.

|	FWHM (ppm)	δ (ppm)
SnO_2 solvothermal synthesis	5.1	-603.9
SnO_2 hydrothermal synthesis	6.5	-604.4
SnO_2 sol-gel synthesis	5.5	-602.6

MAS NMR measurements were made to study the Sn-O bounds (Figure 5, Table 3). The chemical shifts of SnO_2 in ^{119}Sn NMR are well known. Clayden et al. established values of -604.3 ppm for covalent Sn-O [25] synthetized by standard high-temperature solid state reaction methods. They highlighted the wide range of chemical shifts observed for different tin oxides, suggesting a sensitivity to the local environment. Cossement et al. obtained -603 ppm for commercial covalent Sn-O materials [37]. For our samples, chemical shifts between -602.6 and -604.4 ppm were obtained. Broad lines related to a strong local disorder are observed for all three materials. For solvo and hydrothermal ones, this may be due to the occupation of anionic sites by OH^- or O_2^- anions. The shoulder line is observed for solvo and hydrothermal materials at about -610 ppm. Chen et al. reported that this peak is derived from surface Sn species that are close to absorbed water molecules and hydroxyl groups [38]. This is consistent with the observation of the Sn-OH bond identified by infrared for solvo and hydrothermal materials. For aerogel material, a shift of the Sn-O band is observed. This phenomenon is characteristic of paramagnetic contributions due to the appearance of vacancies around the tin site. The result was observed for ^{19}F MAS NMR by Li et al. in the case of $TiOF_2$ with presence of OH groups [39] or ionosorbed forms of oxygen (O^{2-}, O^-)for [17]O by Ren et al. in the case of TiO_2 particles [40] or Sn^{3+} formation.

Electron Spin Resonance (ESR) confirms these paramagnetic centers. The signal observed at g= 1.89 (ΔH=371.5 mT) corresponds to the intrinsic defects of SnO_2 (FigSI1). The intensity and shape of this signal depend on the synthesis conditions of the SnO_2 samples. Ivanovskaya et al. studied the nature of paramagnetic tin oxide defects obtained by the sol-gel method and by heat-treatment.

They conclude that the presence of stable paramagnetic centers with $g \ll g_e$ occurs in non-stoichiometric SnO_{2-x} ($x<2$) oxide with formation of Sn^{2+} ions, SnO/SnO_2 layered structure and oxygen vacancies V_o: $[Sn^{2+} - V_o - Sn^{4+}]$. Oxygen vacancies can act as electron trapping centers and lead to adverse electrochemical performance [41].

3.4 Electrochemical properties

Galvanostatic measurements at 10 mA.g^{-1} were performed for all three materials. The first galvanostatic cycle and cycling performance of the material considering the mass of the active material SnO_2 only are shown in Figure 6. Conversion type materials have been extensively investigated for lithium-ion battery applications. Theoretically, SnO_2 will react with lithium in two steps. First, conversion occurs with the formation of amorphous Li_2O (Figure 6a from (1) to (3)), and then the alloying reaction takes place (Figure 6b from (3) to (4)) [8].
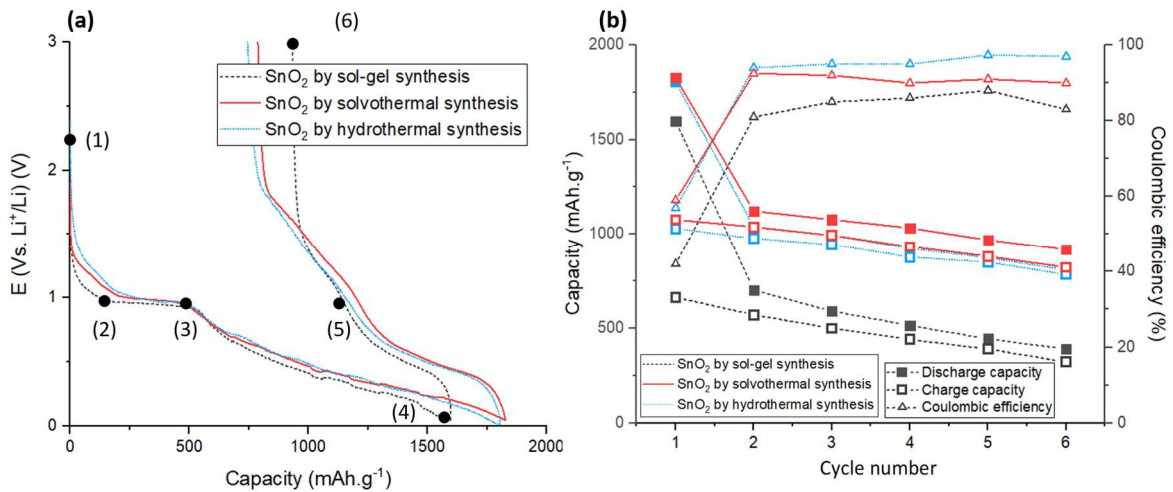
Figure 6 : (a) First Discharge/Charge curve of SnO_2 particles at 10 mA.g^{-1} prepared under various conditions. (b) Comparative cycling performance of the materials owing to discharge. Coulombic efficiency of the materials.

All three materials have a similar first cycle shape. An observed plateau ($\approx$1V) in Figure 6a from (2) to (3) can be attributed to the redox process of Sn (IV) to Sn metal. It has been shown that the length of this plateau depends on the amount of Li_2O formed [42]. The plateau can be observed for all three materials, however, the length of the plateau, the capacity of the first discharge/charge and the irreversibility between them are different. According to the literature, the first reduction and oxidation curves of the materials can be cut as follows:

(1) - (2): Pre-conversion stage

(2) - (3): Main conversion step: $SnO_2 + 4Li^+ + 4e^- \rightarrow Sn + 2Li_2O$

(3) - (4): Alloy formation step: $Sn + xLi^+ + xe^- \rightarrow Li_xSn$ ($0 \leqslant x \leqslant 4.4$)

(4) - (5): Alloy decomposition step: $Li_xSn \rightarrow Sn + xLi^+ + xe^-$ ($0 \leqslant x \leqslant 4.4$)

(5) - (6): Reversible conversion step

Table 4: First galvanostatic discharge/charge gravimetric capacity of SnO_2 obtained by solvothermal, hydrothermal and sol-gel syntheses.

Mechanism		Curve's part	Theoretical capacity for SnO_2 (mAh.g^{-1})	Experimental capacity (mAh.g^{-1}) $\pm$ 10 %		
				Solvothermal	Hydrothermal	Sol-gel
Discharge	Pre conversion	1-2	/	222	282	122
	Conversion	1-3	711	484	512	544
	Alloying	3-4	993	1343	1292	1054
Total discharge		1-4	1705	1827	1804	1598
Charge	Under 1V	4-5	993	705	625	458
	Above 1V	5-6	/	373	405	206

Total charge	4-6	993	1078	1030	664
Coulombic efficiency (%)		58	59	57	42

The theoretical and experimental capacities of each step are shown in Table 4. The gravimetric

capacities obtained for the part of the curve before plateau conversion are 282, 222 and 122

mAh.g^{-1} for the hydrothermal, solvothermal, and sol-gel materials, respectively. Such a difference

can be attributed to the formation of a different compound before 1V. With infrared spectroscopy,

peaks attributed to hydroxyl bound were identified for solvo and hydrothermal materials and could

explain the difference in the galvanostatic first discharge. With regard to this hypothesis, the part of

the curve before the plateau would correspond to the formation of the amorphous phase of LiOH

and will be related to the hydroxyl group contents in the material [43]. However, a smooth profile

with a significant offset before the plateau have been linked to the presence of several discrete

states between the valence band and the conduction band [34]. These states are caused by the

presence of defects in the structure. These defects will weaken the cation-anion bond and facilitate

the rearrangement of the bonds during the insertion of lithium [29].

With regard to the "conversion part" (Figure 6a (1)-(3)), all three materials have a capacity below

the theoretical value for the conversion of SnO_2 to Sn (711 mAh.g^{-1}), 484 mAh.g^{-1}, 512 mAh.g^{-1}

and 544 mAh.g^{-1} for solvothermal, hydrothermal and aerogel materials, respectively. With respect

to our last two assumptions, the difference must be related to a decrease in the theoretical capacity

with

-OH groups, since the theoretical gravimetric capacity of $Sn(OH)_4$ is 574 mAh.g^{-1} instead of 711

mAh.g^{-1} for SnO_2. It can also be correlated with the arbitrary limit of conversion end before the

alloying process. Indeed, at the end of the first cycle, the coulombic efficiencies are 59%, 57% and

41% for the solvothermal, hydrothermal and aerogel materials, close to the theoretical value of 58%

considering only the alloy as reversible.   In another way, Courtney et al. and Liu et al. have related

the length of the conversion plateau to the size of the crystallites [28,44]. Indeed, a small crystallite

size will limit the cohesion of two phases and thus the observation of plateau in electrochemistry.

The voltage at which the conversion mechanism occurs is not yet clear. Recently, Böhme et al.

have made great progress in understanding the SnO_2 mechanism, using XPS and HAXPES. They

have shown that the conversion reaction overlaps with the alloy reaction [45]. Kim et al. obtained

similar results by X-ray adsorption, but showed some dependencies between the conversion and

the bond strength of the material [13]. For the alloyed portion (Figure 6a from (3) to (4)) of the

materials, the capacities obtained are much higher than the theoretical capacity. This is consistent

with an overlap of the conversion on the alloy part. However, considering the whole discharge

curve, additional capacity is still observed for the solvo and hydrothermal materials. Indeed, when

the theoretical conversion plus alloy capacity is 1705 mAh.g^{-1}, the solvo and hydrothermal

capacities are 1827 mAh.g^{-1} and 1804 mAh.g^{-1}, respectively. The additional electrons from the first

discharge may result from the formation of a passivation film (SEI). The mechanism of SEI

formation is not yet clear for SnO_2 particles. The phenomena were observed by Beaulieu et al. by

in-situ AFM of a tin electrode at a potential higher than about 0.7V [46]. Moreover, Ehinon et al.

showed by XPS that SEI layer is formed in the case of Ni_3Sn_4 at the first step of discharge [47]. For

SnO_2, Böhme et al. showed that the SEI layer is formed continuously during the reduction of the

first cycle at potentials below 1.2V [45]. During the first charge, a gentle slope of the voltage curve

is observed above 1V. It is known that tin alloying reaction occurs below 1V [42], so the part of the

profile above 1V may explain the extra capacity observed for solvo and hydrothermal compounds. This additional capacity has already been observed in many studies on conversion materials, but its origin is still subject to debate [13,14,48]. The partial reversibility of the conversion reaction was considered as an assumption to the additional capacity. Hu et al. have shown, using NMR and synchrotron in situ techniques, that the extra capacity observed in the case of rutile RuO_2 particles with some -OH groups present on the external and internal surfaces, is due to the generation of LiOH and its subsequent reversible reaction with lithium to form Li_2O and LiH [43]. Lee et al. drew the same conclusion for SnO_2 using in situ TEM analyses [12]. However, using synchrotron analyses, Böhme et al. showed the continuous formation of a SEI layer during the first discharge and its partial dissolution during the next charge [45]. It is well known that the smaller the particle size, the larger the specific surface area, which allows a higher solid electrolyte interface formation (SEI). In addition, the decomposition of the electrolyte leads to a high capacity during the initial discharge [10]. The aerogel has the largets particle size (and smallest specific surface area) and the smallest additional capacity compared to the theory. This could be explained by the formation of a smaller SEI for this material (smaller SSA). However, aerogel obtains the highest irreversibility during the first cycle compared to other materials, which is not consistent with the formation of an irreversible interface.

The presence of OH groups identified by IR and NMR and additional capacity during the first cycles in the case of solvo and hydrothermal materials appears to be consistent with partial reversibility of the conversion. In addition, the capacity before the plateau identified as being dependent on OH content is proportional to the capacity obtained above 1V during charge. Another indication that the additional capacity comes from partial conversion more than SEI is the

irreversibility of the aerogel.

The capacities and coulombic efficiencies of the materials over the first six cycles are shown in Figure 6b. Two types of mechanisms have been identified with electrochemistry. Solvo and hydrothermal syntheses lead to a material whose capacity is better stabilized than that of sol-gel. The hydroxyl groups identified by IR appear to be beneficial to the material and lead to a partial reversible conversion of the amorphous matrix. The higher porosity and specific surface area are also beneficial to electrolyte diffusion and shorten the transport distance of Li ions, which is an advantage for rate capability. In addition, the void space provided by the pores can attenuate the effect of volume change during the repeated charge–discharge cycle process, resulting in better capacity retention. The morphology of the material may explain the slight difference between solvo and hydrothermal materials.

Indeed, TEM images showed that the solvothermal particles are elongated in nanorods. This structure may provide a better means of lithium diffusion [49]. More, SnO_2 nanorods structure can help to alleviate the volume change during the alloying and dealloying reactions [50,51].

The additional capacity observed for the first cycle can be maintained for the first cycles but performance dropped during cycle, probably due to the large volume change resulting in coarsening and delamination. In the case of the aerogel material, the conversion plateau is as long as in the solvo and hydrothermal cases but the alloy part seems to be cut. Significant irreversibility is achieved between discharge and charge. While the hydroxyl group seems to be an advantage for solvo and hydrothermal materials, it cannot fully explain the low capacity and poor reversibility of aerogel. Another possible answer could be the tin environment. Using NMR, we have shown that the Sn-O band related to the aerogel material is shifted compared to that of solvo and hydrothermal

materials. This shift is characteristic of paramagnetic contributions, which may come from vacancies, Sn^{3+} or ionosorbed species in the material. Thus, paramagnetic sites reflect a disordered environment around tin, and we can see a correlation with decreasing performance of tin oxide. These paramagnetic sites are highly reactive sites and will be the first sites to react electrochemically. They can be engaged in electrochemical mechanisms different from the desired ones and can act as lithium diffusion blocking sites for the desired electrochemical mechanisms. Operando ESR could be interesting to perform in order to confirm such hypothesis.

3.5 Heat--treatment of sol-gel material

The sol-gel material had the worst half-cell performance. With respect to the NMR results, it was hypothesized that paramagnetic centers were limiting for this material. In order to increase performance and to confirm the previously formulated hypothesis, a heat-treatment was performed on the material. High temperature treatments are well known as a tool for modifying physico-chemical properties. In the case of aerogel, we expected to decrease cell parameters, reduce SSA and porosity, increase crystallite and particle sizes and limit local disorder.

TEM images and particles size distribution of SnO_2 particles depending on the treatment temperature are given in Figure 7. The microstructure at 600°C and 1000°C is similar. However, the material treated at 1000°C has a larger grain size and a larger size distribution. The average particle size is 16.7 ± 2.6 nm and 40.6 ± 2.1 nm respectively for sol gel heat treated at 600°C and 1000°C.
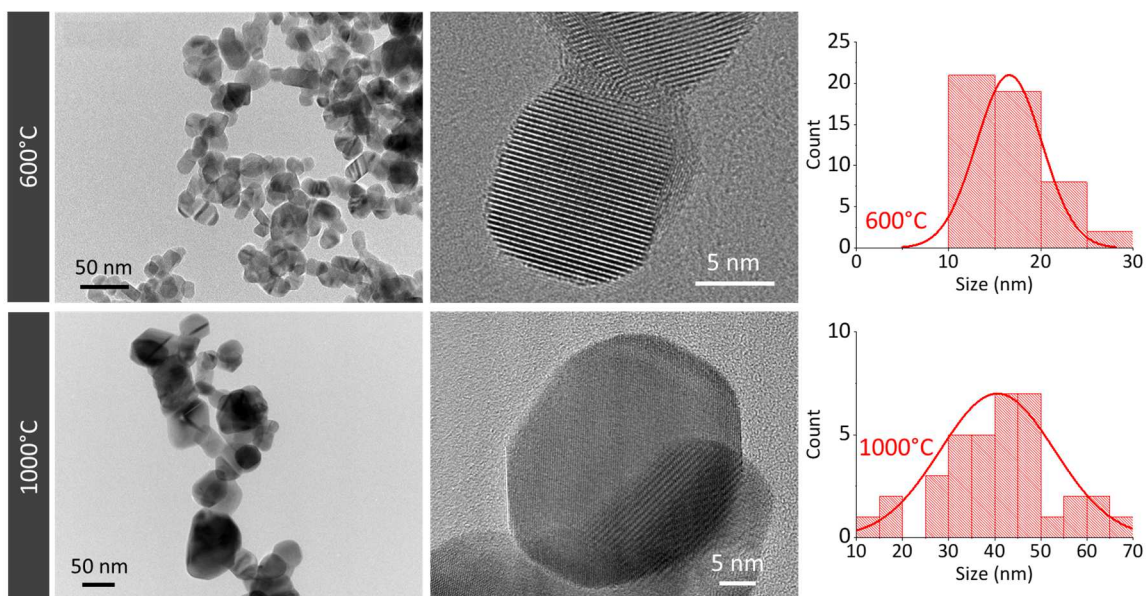
Figure 7: TEM images and particles size distribution of SnO$_2$ nanoparticles prepared by sol-gel method and heat-treated at two different temperatures.

Table 5 : Cells parameters calculated by the Rietveld method, BET specific surface area and total pore volume and NMR values of the material synthesized by sol-gel method and heat-treated at two different temperatures.

| Heat--treat ment temperature	XRD			N$_2$ sorption at 77K				^{119}Sn NMR	
	a = b (Å)	c (Å)	Chi2	BET SSA (m^2.g^{-1})	Volume of micropores < 2 nm (cm^3.g^{-1})	Volume of mesopores [2- 50 nm] (cm^3.g^{-1})	Total porous volume (cm^3.g^{-1})	FWHM (ppm)	δ(Sn-O) (ppm)
600°C	4.7379	3.1871	2.06	35.1 ± 0.1	0.003	0.029	0.089	5.5	-602.6
1000°C	4.7370	3.1865	2.34	7.5 ± 0.1	0.000	0.012	0.021	2.3	-604.1

Table 5 shows the structural and morphological properties of SnO_2 aerogel heat--treated at 600°C and 1000°C. X-ray structural characterizations are in agreement with what was expected, the cell parameter decreases, showing a better organization of the crystalline structure. Regarding N_2 sorption, the porosity decreased considerably with increasing particle size. The aim of the heat-treatment was mainly to reorganize the SnO_2 particles in order to reduce the paramagnetic sites causing interference with NMR measurements. Figure 8 shows the ^{119}Sn NMR spectra of the two heat-treated aerogels at 600°C and 1000°C. The material at 1000°C has a thinner Sn-O band than that at 600°C. In addition, its chemical shift is in line with that of the solvo and hydrothermal materials. We cannot discuss a correlation between paramagnetic centers and electrochemical performance because it seems that these centers are no longer present.
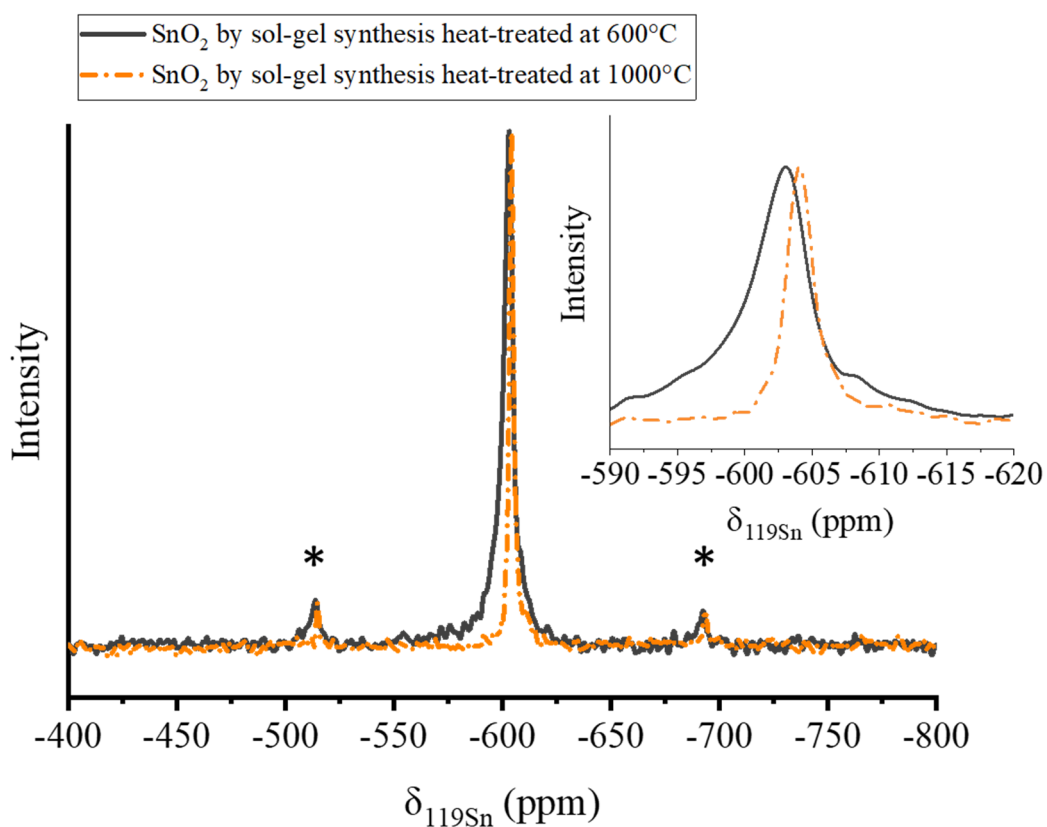
Figure 8: ^{119}Sn solid-state NMR spectra of SnO_2 obtained by sol-gel syntheses heat- treated at 600°C and 1000°C, with spinning sidebands denoted *.

The first discharge and charge curves for the heat-treated SnO_2 aerogel at 600°C and 1000°C are shown in Figure 9a. The theoretical and experimental capacities of the first cycle capacity are shown in Table 6. During discharge, the front part of the plateau does not change after the heat-treatment. This is consistent with the fact that no hydroxyl groups are present in either material. The conversion plateau (Figure 9a (2)-(3)) increases considerably, with a 23% improvement in the conversion part after treatment at 1000°C. The paramagnetic centres observed for the aerogel treated at 600°C disappeared with treatment at 1000°C due to the restructuring of the material (observed by XRD). This result affects the electrochemical properties with a higher Li_2O conversion rate, which explains the improved conversion. The alloy part is improved after the heat-treatment (by 6%). By observing the charge curve, a significant performance improvement of 34% is also observed for the aerogel treated at 1000°C. The reversible alloying process (Figure 9a (4)-(5)) is better, but the most important improvement is in the performance of the charge above 1V with an improvement of 60%. The gravimetric capacity of the first discharge remained below 993 mAh.g^{-1} which leaves doubt as to whether the conversion is reversible or whether the alloy mechanism polarized by the formation of a large amount of Li_2O continues above 1V. However, the gentle slope observed above 1V seems to prove reversible conversion. The capacity and coulombic efficiency of the first cycles are shown in Figure 9b. The capacity of the first cycle has been significantly improved for aerogel heat-treated at 1000°C. However, the coulombic efficiency during the cycle does not change, which could be correlated to poor lithium diffusion during the

discharge.
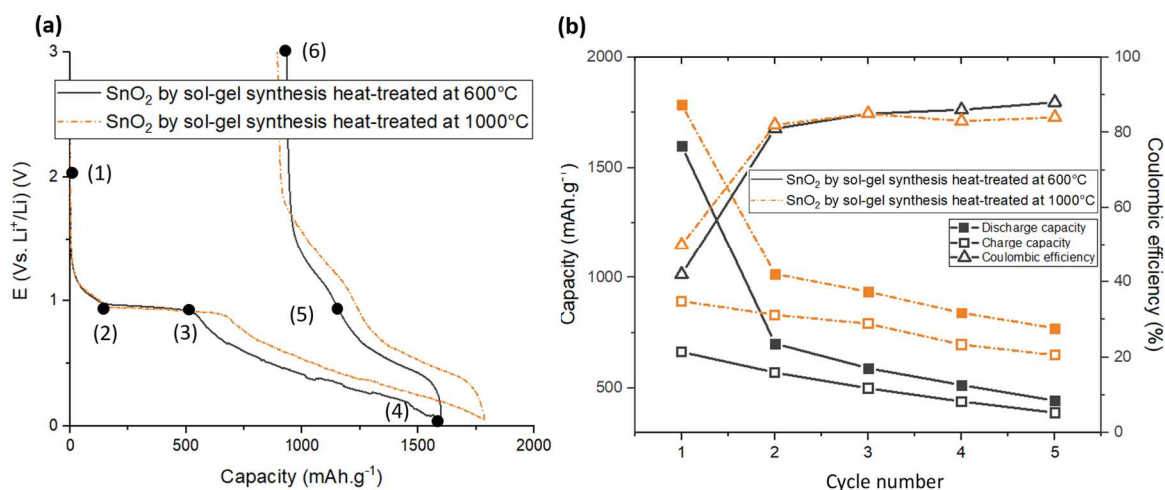
Figure 9 : (a) First Discharge/Charge curve at 10 mA.g^{-1} of SnO$_2$ obtained by sol-gel synthesis particles heat-treated at 600°C and 1000°C. (b) Comparison of cycling performance and coulombic efficiency of the materials at 10 mA.g^{-1}.

Table 6 : First galvanostatic discharge/charge gravimetric capacity for SnO$_2$ obtained by sol-gel synthesis and heat-treated at 600°C and 1000°C.

Mechanism		Curve's part	Theoretical capacity for SnO$_2$ (mAh.g^{-1})	Measured capacity (mAh.g^{-1})		Improvement rate (%)
				600°C	1000°C	
Discharge	Before conversion	1-2	/	122	124	1
	Conversion	1-3	711	544	671	23
	Alloying	3-4	993	1054	1115	6
Total discharge		1-4	1705	1598	1786	12
Charge	Under 1V	4-5	993	458	562	23
	Above 1V	5-6	/	206	331	60

| Total charge | 4-6 | 993 | 664 | 893 | 34 |
| Coulombic efficiency (%) | | 58 | 42 | 50 | 19 |

4. Conclusions

In summary, three different SnO_2 materials have been synthesized. The particles of the materials observed using TEM consist of a single crystal with a nanorod morphology for the solvothermal and spherical morphology for sol-gel and hydrothermal. Due to their nanometric size the presence of significant structural defects was expected. In agreement with this hypothesis, the anisotropy of these materials was demonstrated using ^{119}Sn NMR by the presence of wide band characteristic of the Sn-O bond of SnO_2. The various chemical shift of this band highlights the presence of paramagnetic centres in the case of sol-gel material (confirmed by ESR).

In the case of solvothermal and hydrothermal, different structural defects were observed compared to the sol-gel one. Indeed, using infrared spectroscopy many OH groups covalently bounded to tin were observed.

While the hydroxyls seem to be beneficial for electrochemical performance, the opposite has been observed for paramagnetic centres. However, heat-treatment at 1000°C allowed to align the chemical shift of the Sn-O line observed by NMR with solvothermal and hydrothermal materials and to saturate paramagnetic centres. The heat-treatment also improved the capacity of the first cycles.

Moreover, it allows to prove that the presence of paramagnetic centres is critical for the electrochemical performances. Indeed, aerogel heat-treated at 1000°C has better electrochemical performance than the one heat treated at 600°C. Unfortunately, aerogel treated at 1000°C has poor

reversibility and low coulombic efficiency compared to solvothermal and hydrothermal materials, probably due to two factors, the presence of larger particles size and the absence of OH groups on the material.

Finally, for the hydro and solvothermal material, the particle shapes play a role in performance. The solvothermal material has nanorod-shaped particles which favors the electrons transport and therefore the electrochemical performance compared to the spherical shape material.

Minimizing the crystallites size and controlling the type of defect are key factors for obtaining a very high capacity SnO_2 material up to 900 mAh.g^{-1} and limited irreversibility during the first cycles. However, the large volume change during charge and discharge, and the coarsening of tin particles limit the performance upon cycling. Numerous studies have demonstrated the benefits of adding SnO_2 to the carbon matrix to increase electronic conductivity and to prevent coalescence of tin particles. For example, Jahel et al. showed that confinement of SnO_2 particles in the pores of a mesoporous carbon prevented particles agglomeration and limited volume changes. This method allowed a capacity of 443 mAh.g^{-1} after 2000 cycles with a coulombic efficiency of almost 100% [52]. Also, Zhang et al. report ultrasmall Sn nanoparticles embedded in spherical hollow carbon with a high Li-storage capacity (743 mAh.g^{-1} at 0.5 mA.g^{-1}) and extremely high cyclic stability (92.1% capacity retention after 6000 cycles at 4 mA.g^{-1}) [53].

However, keys parameters have yet to be studied and understood for SnO_2/carbon composite materials but we believe that step-by-step study focusing on the chemistry and intrinsic characteristics of the materials will allow the commercial use of tin oxide.

References

[1]   J.M. Tarascon, M. Armand, Issues and challenges facing rechargeable lithium batteries, Nature. 414 (2001) 359–367. https://doi.org/10.1038/35104644.

[2]   D. Andre, H. Hain, P. Lamp, F. Maglia, B. Stiaszny, Future high-energy density anode materials from an automotive application perspective, J. Mater. Chem. A. 5 (2017) 17174–17198. https://doi.org/10.1039/C7TA03108D.

[3]   J. Cabana, L. Monconduit, D. Larcher, M.R. Palacín, Beyond intercalation-based Li-ion batteries: the state of the art and challenges of electrode materials reacting through conversion reactions, Adv. Mater. Deerfield Beach Fla. 22 (2010) E170-192. https://doi.org/10.1002/adma.201000717.

[4]   P. Poizot, S. Laruelle, S. Grugeon, L. Dupont, J.-M. Tarascon, Nano-sized transition-metal oxides as negative-electrode materials for lithium-ion batteries, Nature. 407 (2000) 496–499. https://doi.org/10.1038/35035045.

[5]   X. Bian, Y. Dong, D. Zhao, X. Ma, M. Qiu, J. Xu, L. Jiao, F. Cheng, N. Zhang, Microsized Antimony as a Stable Anode in Fluoroethylene Carbonate Containing Electrolytes for Rechargeable Lithium-/Sodium-Ion Batteries, ACS Appl. Mater. Interfaces. 12 (2020) 3554–3562. https://doi.org/10.1021/acsami.9b18006.

[6]   C.J. Pelliccione, E.V. Timofeeva, C.U. Segre, Potential-Resolved In Situ X-ray Absorption Spectroscopy Study of Sn and SnO2 Nanomaterial Anodes for Lithium-Ion Batteries, J. Phys. Chem. C. 120 (2016) 5331–5339. https://doi.org/10.1021/acs.jpcc.5b12279.

[7]   C.J. Wen, R.A. Huggins, Thermodynamic Study of the Lithium-Tin System, J. Electrochem. Soc. 128 (1981) 1181. https://doi.org/10.1149/1.2127590.

[8]   I.A. Courtney, J.R. Dahn, Electrochemical and In Situ X-Ray Diffraction Studies of the Reaction of Lithium with Tin Oxide Composites, J. Electrochem. Soc. 144 (1997) 2045–2052. https://doi.org/10.1149/1.1837740.

[9]   D. Deng, Li-ion batteries: basics, progress, and challenges, Energy Sci. Eng. 3 (2015) 385–418. https://doi.org/10.1002/ese3.95.

[10] C. Kim, M. Noh, M. Choi, J. Cho, B. Park, Critical Size of a Nano SnO2 Electrode for Li-Secondary Battery, Chem. Mater. 17 (2005) 3297–3301. https://doi.org/10.1021/cm048003o.

[11] Q. Zhao, L. Ma, Q. Zhang, C. Wang, X. Xu, SnO2-Based Nanomaterials: Synthesis and Application in Lithium-Ion Batteries and Supercapacitors, J. Nanomater. (2015). https://doi.org/10.1155/2015/850147.

[12] S.-Y. Lee, K.-Y. Park, W.-S. Kim, S. Yoon, S.-H. Hong, K. Kang, M. Kim, Unveiling origin

of additional capacity of SnO2 anode in lithium-ion batteries by realistic ex situ TEM analysis, Nano Energy. 19 (2016) 234–245. https://doi.org/10.1016/j.nanoen.2015.10.026.

[13] H. Kim, D.-S. Yang, J.H. Um, M. Balasubramanian, J. Yoo, H. Kim, S.B. Park, J.M. Kim, W.-S. Yoon, Comparative study of bulk and nano-structured mesoporous SnO2 electrodes on the electrochemical performances for next generation Li rechargeable batteries, J. Power Sources. 413 (2019) 241–249. https://doi.org/10.1016/j.jpowsour.2018.12.035.

[14] R. Hu, D. Chen, G. Waller, Y. Ouyang, Y. Chen, B. Zhao, B. Rainwater, C. Yang, M. Zhu, M. Liu, Dramatically enhanced reversibility of Li2O in SnO2-based electrodes: the effect of nanostructure on high initial reversible capacity, Energy Environ. Sci. 9 (2016) 595–603. https://doi.org/10.1039/C5EE03367E.

[15] D. Cao, H. Gu, C. Xie, B. Li, H. Wang, C. Niu, Binding SnO2 nanoparticles onto carbon nanotubes with assistance of amorphous MoO3 towards enhanced lithium storage performance, J. Colloid Interface Sci. 504 (2017) 230–237. https://doi.org/10.1016/j.jcis.2017.05.056.

[16] S.-W. Hwang, S.-H. Hyun, Synthesis and characterization of tin oxide/carbon aerogel composite electrodes for electrochemical supercapacitors, J. Power Sources. 172 (2007) 451–459. https://doi.org/10.1016/j.jpowsour.2007.07.061.

[17] Y. Deng, C. Fang, G. Chen, The developments of SnO2/graphene nanocomposites as anode materials for high performance lithium ion batteries: A review, J. Power Sources. 304 (2016) 81–101. https://doi.org/10.1016/j.jpowsour.2015.11.017.

[18] Z. Sun, T. Liao, L. Kou, Strategies for designing metal oxide nanostructures, Sci. China Mater. 60 (2017) 1–24. https://doi.org/10.1007/s40843-016-5117-0.

[19] D. Mohanta, M. Ahmaruzzaman, Tin oxide nanostructured materials: an overview of recent developments in synthesis, modifications and potential applications, RSC Adv. 6 (2016) 110996–111015. https://doi.org/10.1039/C6RA21444D.

[20] R. Retoux, T. Brousse, D.M. Schleich, High-resolution electron microscopy investigation of capacity fade in SnO2 electrodes for lithium-ion batteries, J. Electrochem. Soc. 146 (1999) 2472–2476. https://doi.org/10.1149/1.1391957.

[21] H. Li, Q. Su, J. Kang, M. Huang, M. Feng, H. Feng, P. Huang, G. Du, Porous SnO2 hollow microspheres as anodes for high-performance lithium ion battery, Mater. Lett. 217 (2018) 276–280. https://doi.org/10.1016/j.matlet.2018.01.015.

[22] A. Dieguez, Romano-Rodrguez A., J.R. Morante, J. Kappler, N. Barsan, W. Gopel, Nanoparticle engineering for gas sensor optimisation: improved sol-gel fabricated nanocrystalline SnO_2 thick film gas sensor for NO_2 detection by calcination, catalytic metal introduction and grinding treatments, Sens. Actuators B Chem. 60 (1999) 125–137.

[23] G. Ozouf, G. Cognard, F. Maillard, M. Chatenet, L. Guétaz, M. Heitzmann, P.A. Jacques, C. Beauger, Sb-Doped SnO2 Aerogels Based Catalysts for Proton Exchange Membrane Fuel Cells: Pt Deposition Routes, Electrocatalytic Activity and Durability, J. Electrochem. Soc. 165 (2018) F3036–F3044. https://doi.org/10.1149/2.0041806jes.

[24] G. Ozouf, C. Beauger, Niobium- and antimony-doped tin dioxide aerogels as new catalyst supports for PEM fuel cells, J. Mater. Sci. 51 (2016) 5305–5320. https://doi.org/10.1007/s10853-016-9833-7.

[25] N.J. Clayden, C.M. Dobson, A. Fern, High-resolution solid-state tin-119 nuclear magnetic resonance spectroscopy of ternary tin oxides, J. Chem. Soc. Dalton Trans. (1989) 843–847.

https://doi.org/10.1039/DT9890000843.

[26] C. Marino, J. Fullenwarth, L. Monconduit, B. Lestriez, Diagnostic of the failure mechanism in NiSb2 electrode for Li battery through analysis of its polarization on galvanostatic cycling, Electrochimica Acta. 78 (2012) 177–182. https://doi.org/10.1016/j.electacta.2012.05.126.

[27] F.C. Vásquez, F. Paraguay-Delgado, J.E. Morales-Mendoza, W. Antunez, D. Lardizabal, G. Alonso-Nuñez, G. Berhault, Shape and size controlled growth of SnO2 nano-particles by efficient approach, Superlattices Microstruct. 90 (2015). https://doi.org/10.1016/j.spmi.2015.12.014.

[28] I.A. Courtney, J.R. Dahn, Key Factors Controlling the Reversibility of the Reaction of Lithium with SnO2 and Sn2 BPO 6 Glass, J. Electrochem. Soc. 144 (1997) 2943–2948. https://doi.org/10.1149/1.1837941.

[29] G. Campet, S.J. Wen, S.D. Han, M.C.R. Shastry, J. Portier, C. Guizard, L. Cot, Y. Xu, J. Salardenne, Reversible electrochemical insertion of lithium in fine-grained polycrystalline thin films of mixed-valency metal oxides: application to LixFe2O3 thin film electrodes prepared by the sol-gel process, Mater. Sci. Eng. B. 18 (1993) 201–208. https://doi.org/10.1016/0921-5107(93)90132-7.

[30] W. Zeng, H. Zhang, Y. Li, W. Chen, Z. Wang, Hydrothermal synthesis of hierarchical flower-like SnO2 nanostructures with enhanced ethanol gas sensing properties, Mater. Res. Bull. 57 (2014) 91–96. https://doi.org/10.1016/j.materresbull.2014.05.019.

[31] F.C. Vásquez, F. Paraguay-Delgado, J.E. Morales-Mendoza, W. Antunez, D. Lardizabal, G. Alonso-Nuñez, G. Berhault, Shape and size controlled growth of SnO2 nano-particles by efficient approach, Superlattices Microstruct. 90 (2015). https://doi.org/10.1016/j.spmi.2015.12.014.

[32] A. Grosman, C. Ortega, Capillary condensation in porous materials. Hysteresis and interaction mechanism without pore blocking/percolation process, Langmuir ACS J. Surf. Colloids. 24 (2008) 3977–3986. https://doi.org/10.1021/la703978v.

[33] C. Geoffroy, G. Campet, F. Menil, J. Portier, J. Salardenne, G. Couturier, Optical and Electrical Properties of SnO2:F Thin Films Obtained by R.F. Sputtering With Various Targets, Act. Passive Electron. Compon. 14 (14) e85965. https://doi.org/10.1155/1991/85965.

[34] C.W. Kwon, G. Campet, J. Portier, A. Poquet, L. Fournès, C. Labrugère, B. Jousseaume, T. Toupance, J.H. Choy, M.A. Subramanian, A new single molecular precursor route to fluorine-doped nanocrystalline tin oxide anodes for lithium batteries, Int. J. Inorg. Mater. 3 (2001) 211–214. https://doi.org/10.1016/S1466-6049(01)00021-6.

[35] D. Amalric-Popescu, F. Bozon-Verduraz, Infrared studies on SnO2 and Pd/SnO2, Catal. Today. 70 (2001) 139–154. https://doi.org/10.1016/S0920-5861(01)00414-X.

[36] P.G. Harrison, A. Guest, Tin oxide surfaces. Part 17.—An infrared and thermogravimetric analysis of the thermal dehydration of tin(IV) oxide gel, J. Chem. Soc. Faraday Trans. 1 Phys. Chem. Condens. Phases. 83 (1987) 3383–3397. https://doi.org/10.1039/F19878303383.

[37] C. Cossement, J. Darville, J.-M. Gilles, J.B. Nagy, C. Fernandez, J.-P. Amoureux, Chemical shift anisotropy and indirect coupling in SnO2 and SnO, Magn. Reson. Chem. 30 (1992) 263–270. https://doi.org/10.1002/mrc.1260300313.

[38] J. Chen, X.-P. Wu, L. Shen, Y. Li, D. Wu, W. Ding, X.-Q. Gong, M. Lin, L. Peng, Identification of different tin species in SnO2 nanosheets with 119Sn solid-state NMR spectroscopy, Chem. Phys. Lett. 643 (2016) 126–130.

https://doi.org/10.1016/j.cplett.2015.11.035.

[39] W. Li, M. Body, C. Legein, D. Dambournet, Identify OH groups in TiOF2 and their impact on the lithium intercalation properties, J. Solid State Chem. 246 (2017) 113–118. https://doi.org/10.1016/j.jssc.2016.11.010.

[40] Y. Ren, Z. Liu, F. Pourpoint, A.R. Armstrong, C.P. Grey, P.G. Bruce, Nanoparticulate TiO2(B): an anode for lithium-ion batteries, Angew. Chem. Int. Ed Engl. 51 (2012) 2164–2167. https://doi.org/10.1002/anie.201108300.

[41] M. Ivanovskaya, E. Ovodok, V. Golovanov, The nature of paramagnetic defects in tin (IV) oxide, Chem. Phys. 457 (2015) 98–105. https://doi.org/10.1016/j.chemphys.2015.05.023.

[42] C. Gervillié, A. Boisard, J. Labbé, S. Berthon-Fabry, K. Guérin, Influence of oxygen content in Sn-based negative electrode upon cycling in lithium-ion battery, Mater. Energy. (2020).

[43] Y.-Y. Hu, Z. Liu, K.-W. Nam, O.J. Borkiewicz, J. Cheng, X. Hua, M.T. Dunstan, X. Yu, K.M. Wiaderek, L.-S. Du, K.W. Chapman, P.J. Chupas, X.-Q. Yang, C.P. Grey, Origin of additional capacities in metal oxide lithium-ion battery electrodes, Nat. Mater. 12 (2013) 1130–1136. https://doi.org/10.1038/nmat3784.

[44] W. Liu, X. Huang, Z. Wang, H. Li, L. Chen, Studies of Stannic Oxide as an Anode Material for Lithium-Ion Batteries, J. Electrochem. Soc. 145 (1998) 59. https://doi.org/10.1149/1.1838211.

[45] S. Böhme, B. Philippe, K. Edström, L. Nyholm, Photoelectron Spectroscopic Evidence for Overlapping Redox Reactions for SnO2 Electrodes in Lithium-Ion Batteries, J. Phys. Chem. C. 121 (2017) 4924–4936. https://doi.org/10.1021/acs.jpcc.7b01529.

[46] L.Y. Beaulieu, S.D. Beattie, T.D. Hatchard, J.R. Dahn, The Electrochemical Reaction of Lithium with Tin Studied By In Situ AFM, J. Electrochem. Soc. 150 (2003) A419–A424. https://doi.org/10.1149/1.1556595.

[47] K.K.D. Ehinon, S. Naille, R. Dedryvère, P.-E. Lippens, J.-C. Jumas, D. Gonbeau, Ni3Sn4 Electrodes for Li-Ion Batteries: Li−Sn Alloying Process and Electrode/Electrolyte Interface Phenomena, Chem. Mater. 20 (2008) 5388–5398. https://doi.org/10.1021/cm8006099.

[48] S.-Y. Lee, K.-Y. Park, W.-S. Kim, S. Yoon, S.-H. Hong, K. Kang, M. Kim, Unveiling origin of additional capacity of SnO2 anode in lithium-ion batteries by realistic ex situ TEM analysis, Nano Energy. 19 (2016) 234–245. https://doi.org/10.1016/j.nanoen.2015.10.026.

[49] J. Yan, E. Khoo, A. Sumboja, P.S. Lee, Facile Coating of Manganese Oxide on Tin Oxide Nanowires with High-Performance Capacitive Behavior, ACS Nano. 4 (2010) 4247–4255. https://doi.org/10.1021/nn100592d.

[50] H. Wang, Q. Liang, W. Wang, Y. An, J. Li, L. Guo, Preparation of Flower-like SnO2 Nanostructures and Their Applications in Gas-Sensing and Lithium Storage, Cryst. Growth Des. 11 (2011) 2942–2947. https://doi.org/10.1021/cg2001255.

[51] C. Wang, Y. Zhou, M. Ge, X. Xu, Z. Zhang, J.Z. Jiang, Large-Scale Synthesis of SnO2 Nanosheets with High Lithium Storage Capacity, J. Am. Chem. Soc. 132 (2010) 46–47. https://doi.org/10.1021/ja909321d.

[52] A. Jahel, C.M. Ghimbeu, L. Monconduit, C. Vix-Guterl, Confined Ultrasmall SnO2 Particles in Micro/Mesoporous Carbon as an Extremely Long Cycle-Life Anode Material for Li-Ion Batteries, Adv. Energy Mater. 4 (2014) 1400025. https://doi.org/10.1002/aenm.201400025.

[53] N. Zhang, Y. Wang, M. Jia, Y. Liu, J. Xu, L. Jiao, F. Cheng, Ultrasmall Sn nanoparticles embedded in spherical hollow carbon for enhanced lithium storage properties, Chem.